ELSEVIER ELSEVIER

Contents lists available at ScienceDirect

Earth and Planetary Science Letters

journal homepage: www.elsevier.com/locate/epsl



Extreme seismic anisotropy indicates shallow accumulation of magmatic sills beneath Yellowstone caldera



Sin-Mei Wu^{a,b,*}, Hsin-Hua Huang^{c,d}, Fan-Chi Lin^a, Jamie Farrell^a, Brandon Schmandt^e

- ^a Dept. of Geology and Geophysics, University of Utah, Salt Lake City, UT, USA
- ^b Swiss Seismological Service (SED), ETH Zurich, Switzerland
- c Institute of Earth Sciences, Academia Sinica, Taipei, Taiwan
- ^d Dept. of Geosciences, National Taiwan University, Taipei, Taiwan
- ^e Dept. of Earth and Planetary Sciences, The University of New Mexico, Albuquerque, NM, USA

ARTICLE INFO

Article history:

Received 12 January 2023

Received in revised form 24 April 2023

Accepted 23 May 2023 Available online 8 June 2023

Editor: H. Thybo

Dataset link: https://doi.org/10.7914/SN/WY

Dataset link: https://doi.org/10.7914/SN/MB

Dataset link: https://ds.iris.edu/mda/PB/

Dataset link: https://doi.org/10.7914/SN/US

Dataset link: https://doi.org/10.7914/vztw-bx83

Keywords:
Yellowstone
magmatic sills
radial anisotropy
large-N array
ambient noise tomography

ABSTRACT

Understanding the distribution and mobility of crystal mushes within modern magmatic systems is crucial to volcanic hazard assessments as distinct pockets of mobile magma may become interconnected and lead to melt accumulation on shorter time scales than magma that is broadly distributed in a homogeneous mush. Here, we reveal that Yellowstone's upper-crustal magma reservoir in the top 20 km is heterogeneous in both melt concentration and texture. We exploit ambient noise in an unprecedented dense temporary seismic network to jointly constrain vertically- and horizontally-polarized shear wave speeds to create enhanced 3D isotropic and anisotropic shear velocity models. Our models show an exceptionally low-velocity (>20% reduction) layer 4–7 km beneath the surface, situated near the top of the reservoir previously-imaged by earthquake P-wave tomography. The presence of strong radial anisotropy (20%) within this layer indicates the uppermost portion of the modern Yellowstone reservoir is organized as a sill complex, with up to 28% of melt fraction in horizontally-elongated volumes at depths where rhyolite was commonly stored before past eruptions. The findings demonstrate that high-resolution anisotropic imaging through a dense seismic network can constrain both magma distribution and reservoir texture, which are important to understand the evolution and hazard assessment of volcanic systems like Yellowstone.

© 2023 The Author(s). Published by Elsevier B.V. This is an open access article under the CC BY license (http://creativecommons.org/licenses/by/4.0/).

1. Introduction

Since the last caldera-forming eruption at 0.63 Ma, Yellowstone has experienced several smaller-volume eruptive episodes until 70,000 years ago (Christiansen, 2001). Although the current estimates of melt fraction within Yellowstone's upper-crustal silicic magma reservoir are considered non-eruptive (5%–15% from Farrell et al., 2014; Huang et al., 2015, and 32% from Chu et al., 2010), increasing geochemical evidence from Yellowstone indicates that such a dominantly crystalline state could be ephemeral as portions of the mobile magma could concentrate at shallow depths over relatively short time scales (<1kyr) (Stelten et al., 2015; Till et al., 2015; Shamloo and Till, 2019). In addition, a recent seis-

E-mail address: a06859a35@gmail.com (S.-M. Wu).

mic study proposed that the silicic magma reservoir in Yellowstone is organized as a sill complex (Jiang et al., 2018), meaning the reservoir has a large-scale fabric created by distinct horizontally elongated volumes that alter between crystal-poor and crystal-rich. Long-lived magma reservoirs with low average melt fractions may rapidly increase connectivity among subset volumes with low-viscosity magmas and aggregate into short-lived eruptible reservoirs (Eddy et al., 2016; Cashman et al., 2017). Therefore, as opposed to the wide range of prior melt fraction estimates assuming a homogenized magma texture, it is of great importance to evaluate both spatial and textural heterogeneities of the magma reservoir through enhanced imaging of Yellowstone's shallow magmatic system to advance understanding of its ongoing evolution and implications for hazard assessment.

Images of Yellowstone's crustal magmatic system are predominantly shaped by seismic P-wave travel-time tomography studies using local earthquakes (Husen et al., 2004; Farrell et al., 2014),

^{*} Corresponding author at: Swiss Seismological Service (SED), ETH Zurich, Switzerland.

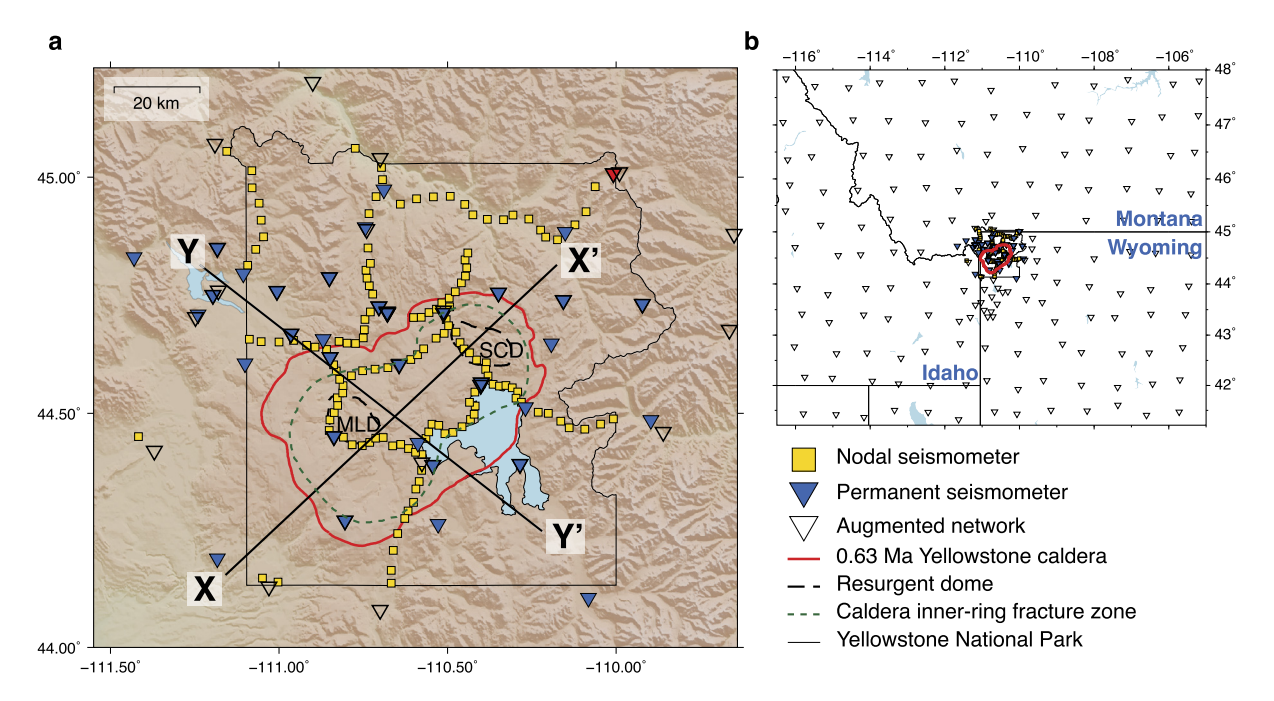


Fig. 1. Maps of Yellowstone volcanic field and seismic stations, (a) An enlargement of the dense array component of the study. Nodal seismometers are shown as yellow squares. Permanent seismic stations near Yellowstone are shown as solid blue triangles. The 0.63 Ma caldera is delineated by the red-solid line. The thin-black line bounds Yellowstone National Park. Mallard Lake (MLD) and Sour Creek (SCD) resurgent domes are outlined by black-dashed lines. The caldera inner-ring fracture zone is depicted as a green-dashed line. The black-solid lines mark the two cross sections shown in Fig. 7. The red triangle marks the virtual source station YNE shown in Fig. 2. (b) the entire seismic network including the sparse array (open triangles) used in this study.

and joint local and teleseismic travel-time tomography (Huang et al., 2015). Along the long axis of the 0.63 Ma caldera, the uppercrustal magma reservoir is illuminated by an elongated, low-VP body \sim 7–18 km depth beneath the surface with an estimated melt fraction of 5-15% and cumulative melt volume of 200-900 km³ (Farrell et al., 2014; Huang et al., 2015). The volume is compatible with two of the three catastrophic eruptions at 1.3 Ma (280 km³) and 0.63 Ma (1000 km³), although eruptions under the current state are unlikely if the melt fraction of 5-15% is evenly distributed within the reservoir. Compared to P-wave velocity, seismic S-wave velocity bears distinct sensitivity to physical properties and can decrease to zero in a melt-dominated medium (e.g., Caricchi et al., 2008). However, the nature of heterogeneity and high attenuation in volcanic fields commonly preclude good-quality S wave observations from earthquake data and consequently V_S models have been less common. Using regional-scale array data, earlier studies have resolved 3D V_S structure of Yellowstone magma body using ambient noise surface wave tomography (Stachnik et al., 2008; Jiang et al., 2018; Maguire et al., 2022a). With the resolution limits imposed by previous array configurations (e.g., Maguire et al., 2022b), prior Vs studies focused on the general properties of the magma reservoir instead of fine-scale heterogeneity within it.

The resolution of tomographic images from earthquake data is commonly limited by the distribution of sources and propagation paths to receivers. In Yellowstone, seismicity usually occurs as seismic swarms (Farrell et al., 2009). Triggered by magmatic fluid migration, prominent swarms in 1985, 2010, and 2017–2018 were located near and outside the northwest rim of the 0.63 Ma caldera (Waite and Smith, 2002; Shelly et al., 2013; Pang et al., 2019). Another distinct swarm with a similar cause that occurred in 2008–2009 was located beneath the northern part of Yellowstone Lake (Farrell et al., 2010). The clustering nature of seismic sources in Yellowstone results in inhomogeneous ray coverage and limited 3D resolution of volumes that may be important in understanding the magmatic system. In contrast to body-wave traveltime tomography, the depth-dependent sensitivity of seismic surface waves at different periods provides a complementary probe

into the shallow magmatic system of Yellowstone. Utilizing seismic interferometry from ambient noise fields, surface wave propagation can be described by a 2D wave equation between source and receiver stations at a given period (Tromp and Dahlen, 1993), with the horizontal ray coverage dictated by the array configuration. A dense array can thus provide denser and importantly, more homogeneous sampling of the 3D shear-velocity structure of the magmatic system.

2. Data and methods

2.1. Dense nodal array and regional seismic networks

In the summer of 2020, we deployed a temporary 650-element 3-component dense nodal array throughout Yellowstone National Park between August 17 and September 21 2020 (Fig. 1; Farrell, 2020). Despite the 5 Hz corner frequency, previous studies have shown the MagSeis Fairfield geophones we used can record passive ambient noise signals up to \sim 10 s period (Wang et al., 2019; Wells et al., 2022). The nodal array had an aperture of \sim 140 km that comprises two spatial scales - a sparse spacing of 1-3 km across the whole area and two dense lines with a spacing of \sim 250 m across the 0.63 Ma caldera. In this study, we use data from the coarser component of the dense array for passive imaging (yellow squares in Fig. 1a). As the nodal array was deployed along accessible roads/trails, we also include permanent stations in the vicinity of the deployment but located in more remote areas to minimize spatial gaps in the path coverage (blue triangles in Fig. 1a). There are 37 permanent stations that coexisted during deployment time with a mixture of short-period and broadband sensors from the Yellowstone Seismic Network (network code: WY), Montana Regional Seismic Network (MB), Plate Boundary Observatory Borehole Seismic Network (PB), and United States National Seismic Network (US). In addition, following Jiang et al. (2018), we use continuous data of 188 stations from USArray Transportable Array (TA) and regional networks across Idaho, Wyoming, and Montana that were operating during 2007-2010 (open triangles in Fig. 1b).

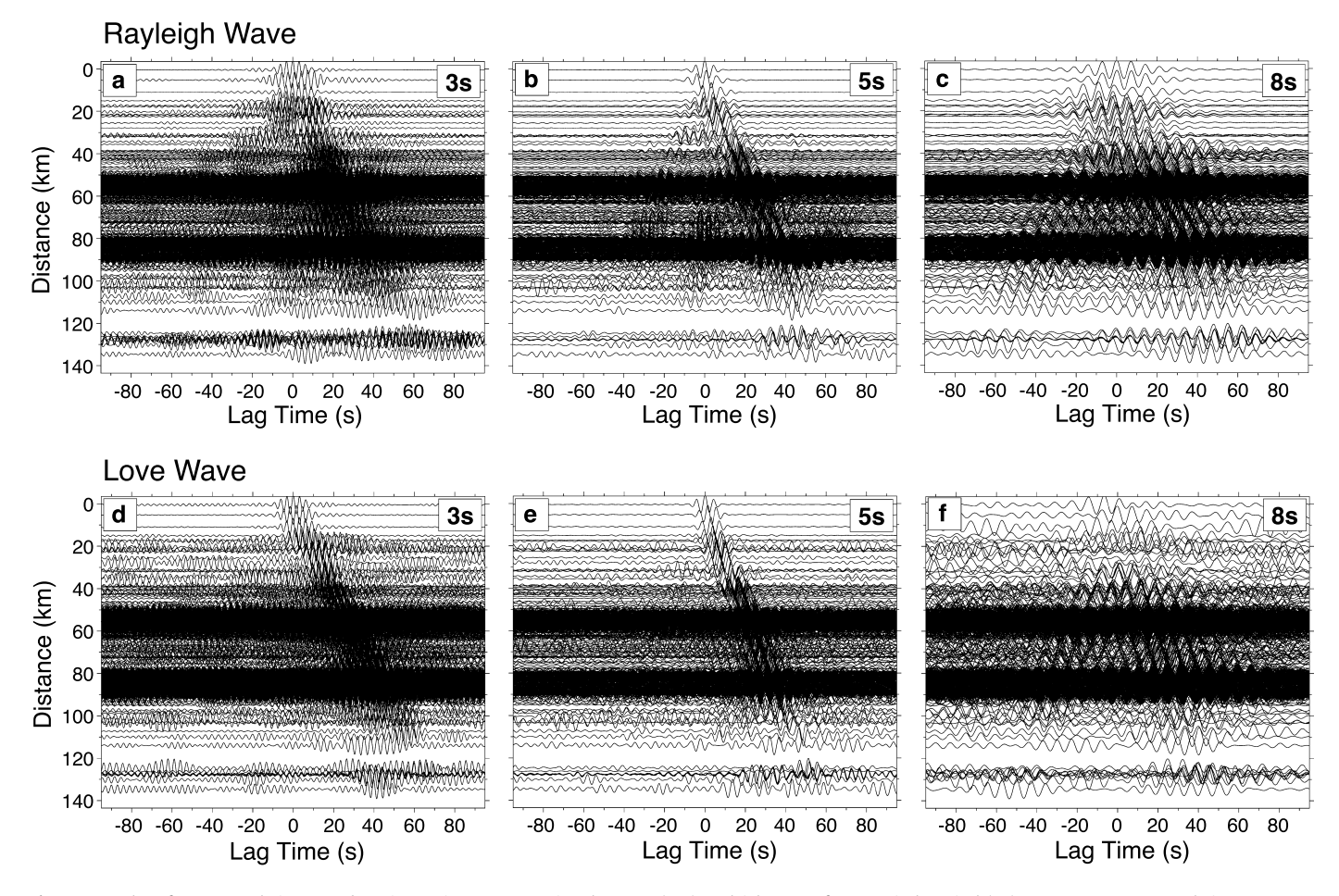


Fig. 2. Examples of cross-correlation record sections using YNE as a virtual source. (a–c) Rayleigh waves from vertical-vertical (ZZ) component cross-correlations at 3-, 5-, and 8-second periods. (d–f) same as (a–c) but for Love waves from transverse-transverse (TT) component cross-correlations.

All the data are accessible via IRIS MetaData Aggregator (https://ds.iris.edu/mda/). Because the data from the TA time window have much larger station spacing (>50 km), for the remainder of the paper, we refer to the TA and concurrent regional networks as the sparse array and the nodal plus nearby permanent stations as the dense array.

2.2. Ambient noise cross-correlation

We use continuous recordings from the dense array to calculate multi-component noise cross-correlations. The following processing is applied: pre-filtering (Butterworth filter bandpass between 0.1 and 33 s periods), removing instrument response, decimating to 50 samples per sec, and splitting into hourly segments. For each segment, we calculate multicomponent cross-correlation (i.e., the combination of vertical (Z), north (N), and east (E)) between all available station pairs after spectral whitening (Lin et al., 2014; Wu et al., 2017). The cross-correlations (CC) are normalized based on their maximum amplitude of vertical-vertical component, linearly stacked through the entire time period to enhance the signal-tonoise ratio (SNR), then the horizontal components are rotated into radial (R) and transverse (T) directions. We use CCs from Jiang et al. (2018) for the sparse array data, which were obtained via similar processes. Note the CC from the sparse array dataset is completely independent of the dense array CC, as many of the sparse array stations had been dismantled before the nodal deployment. The usage of the large-scale array is mainly to serve as a reference background model for phase travel time correction and to provide long-period measurements (i.e., up to 25 s period) for stabilizing the surface wave inversion. Using a virtual source station YNE (Fig. 1a) in the northeast of the array as an example, coherent Rayleigh and Love wave arrivals propagating across the study area can be observed from the vertical-vertical (ZZ) and transverse-transverse (TT) components of the CCs between 3 and 8 sec periods (Fig. 2). The surface waves are stronger in the causal lag time, implying an inhomogeneous noise source distribution, consistent with a previous microseismic study in this region (Koper and Burlacu, 2015). To mitigate potential source distribution bias, we average the causal and acausal parts of the CCs and use the symmetric waveform for the remaining processing (e.g., Lin et al., 2008).

2.3. Dispersion of surface wave phase velocity

The phase travel times and velocities for both Rayleigh and Love waves are measured through frequency-time analysis (FTAN; Fig. S1; Bensen et al., 2007; Lin et al., 2008). Two data selection criteria are applied to ensure only reliable surface wave data are used: an SNR larger than 8 and an interstation distance larger than 1.5 wavelengths assuming a phase velocity of 3 km/s. Limited by the selection criteria and the array geometry, viable periods for surface wave imaging are 3–10 s and 6–25 s for the dense and sparse array, respectively (Fig. 3). Between both arrays, periods at 7 and 8 s have the most abundant measurements for Love and Rayleigh waves, respectively. Therefore, we take these two periods as starting/reference periods for Love and Rayleigh waves, respectively, for correcting 2π ambiguity (cycle skipping) of phase travel time.

For the sparse array dataset, the 2π ambiguity can mostly be resolved in the FTAN process by taking long-period measurements as references and requiring the continuity of the dispersion curves

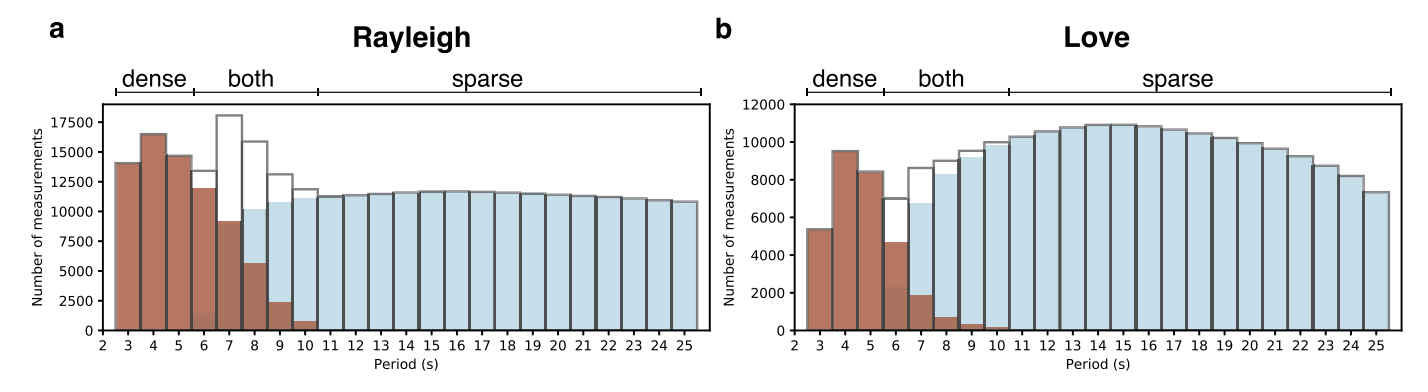


Fig. 3. Number of measurements at different periods. (a) Rayleigh wave and (b) Love wave measurements. The red and blue colors indicate the data from the dense and sparse array, respectively. The opened histograms represent the total data quantity combining both arrays.

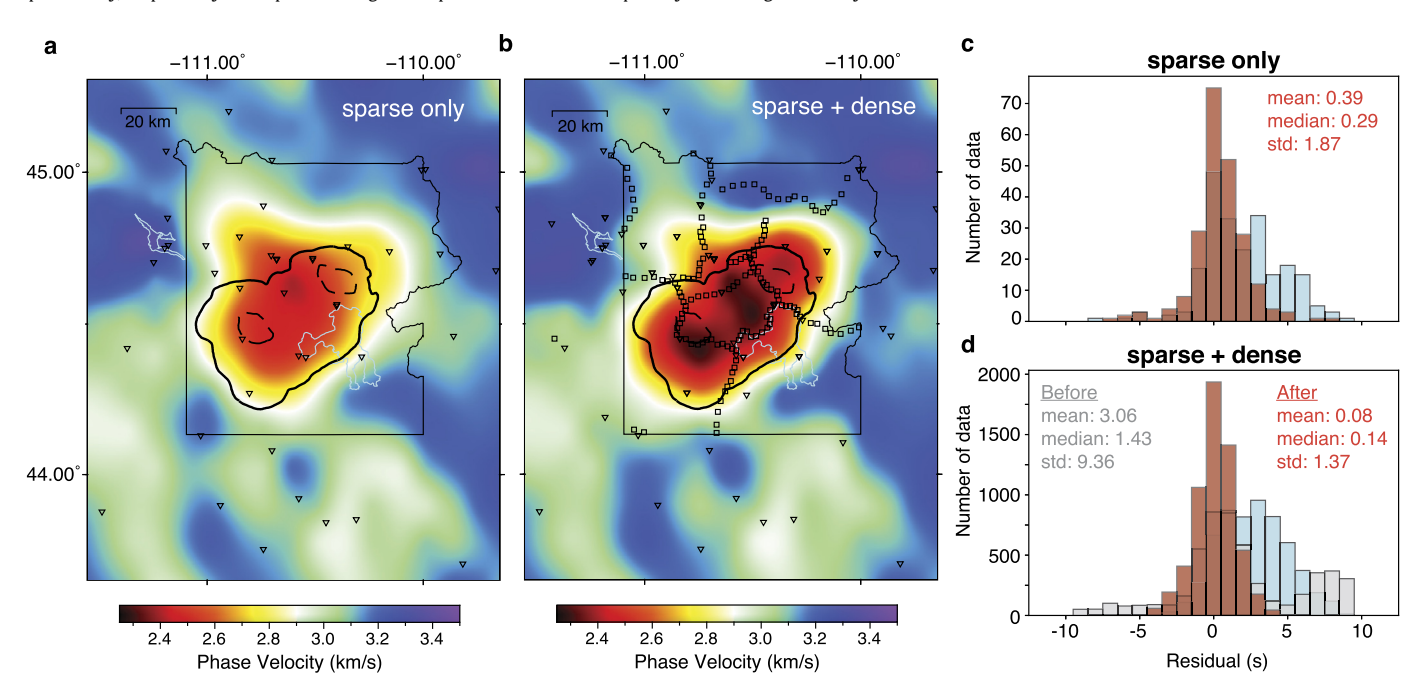


Fig. 4. Comparison of Rayleigh wave phase velocity maps at 8-s period. (a) Phase map using sparse array data only. (b) Phase map combining sparse and dense array data after 2π correction. The open triangles and squares represent seismic stations from the sparse and dense array, respectively. (c) The distribution of travel time residuals before (blue) and after (red) inversion using sparse array data within the area shown in the map. (d) The distribution of travel time residuals before 2π correction combining both sparse and dense array data (gray). The blue and red show the misfit distributions before and after the inversion, respectively, after the 2π correction.

(Lin et al., 2008). For the dense array dataset, no reliable longperiod measurement is available limited by the short ray paths and 1.5 wavelength criterion. Here, we first consider all sparse and dense array travel time data corrected and uncorrected, respectively. Starting at the reference period, we then invert the 2D reference phase velocity map using all corrected data (Barmin et al., 2001). We correct all measurements with 2π jumps such that the predicted and observed travel time differences are smaller than half of a period. These corrected measurements are used to correct for measurements from the same station pair but at the neighboring period assuming the continuity of the dispersion curves. We repeat this process iteratively with small period steps (0.5 s and 0.2 s above and below 6 s period, respectively) to successively correct for all traveltime measurements between 3 and 10 sec period. An example of 2D Rayleigh phase velocity maps at 8-s period is shown in Fig. 4. The 2π correction appears to be effective in reducing overall travel time residuals and the resultant phase map with the dense array data exhibits a slower anomaly well confined beneath the 0.63 Ma caldera, broadly consistent with prior V_P studies (Farrell et al., 2014; Huang et al., 2015). The phase velocity maps at various other periods are shown in Fig. S2.

2.4. Three-dimensional surface wave inversion

To account for the strong lateral and vertical heterogeneity, we apply a one-step ray-tracing-based 3D tomography to invert the surface wave dispersion measurements. Conventional surface wave tomographic methods undergo a two-step process, first obtaining a 2D phase velocity map and then resolving the 1D V_S depth profile at each gridpoint to construct a semi 3D model (e.g., Barmin et al., 2001, Bensen et al., 2007; Berg et al., 2020; Mordret et al., 2015; Lin et al., 2013; Yao et al., 2008). In contrast, the determination of the 3D V_S model via a one-step process has been less common (e.g., Fang et al., 2015, 2016; Golos et al., 2018). The one-step inversion we implement takes into account the 3D wave propagation in the subsurface that avoids potential inconsistency in space introduced by independent inversion/regularization processes between different periods. Furthermore, such a one-step inversion makes 3D resolution tests and future joint surface and body wave inversion possible. After integrating with a ray-tracing-based, off-great-circle propagation, we deem the 3D surface wave tomographic inversion is a more realistic scheme for complex areas, particularly in the volcanic region where over 5% velocity anomalies can be present

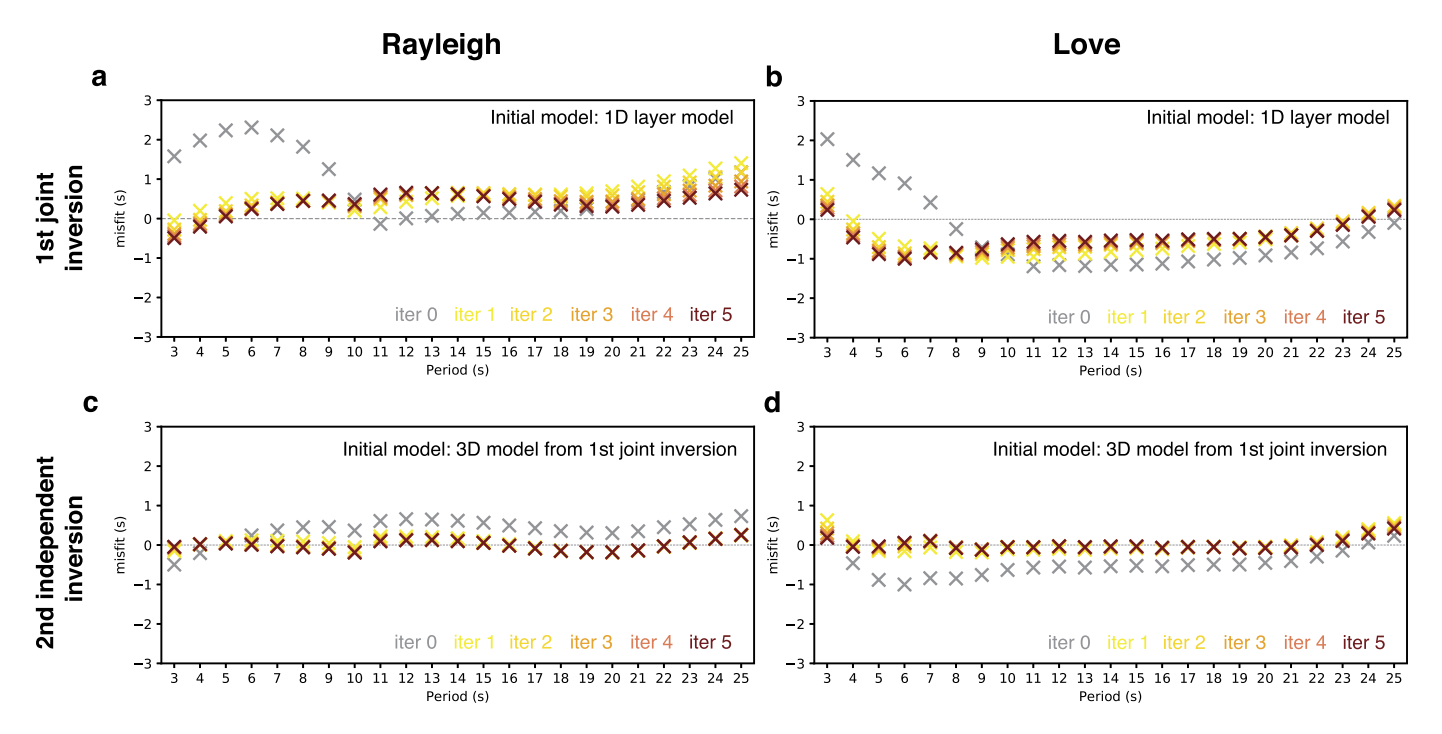


Fig. 5. Misfits as a function of periods from different inversions. (a) and (b) Rayleigh and Love wave misfits from the first step of the joint inversion. (c) and (d) Rayleigh and Love misfits from the second step of the independent Rayleigh-only and Love-only inversions using the resultant 3D model from the joint inversion as the initial model.

(e.g., Farrell et al., 2014; Huang et al., 2015; Jaxybulatov et al., 2014; Mordret et al., 2015; Wang et al., 2017).

Here we briefly summarize the one-step inversion method we implement. Given a reference 3D velocity model, for each surface location, period, and surface wave type, we first calculate the phase velocity and its depth sensitivity (Fig. S3) based on the method of Herrmann and Ammon (2004) assuming a flat Earth. The phase velocities at different locations are then combined to construct the 2D reference phase velocity map. For each source and receiver pair, we adapt the spherical pseudo-bending ray tracing algorithm (Koketsu and Sekine, 1998; Huang et al., 2014) to determine the 2D raypath and calculate the predicted phase travel time. The 1D sensitivity kernels along the ray path are then tri-linearly interpolated to construct the final 3D sensitivity kernel. All measurements from different periods are combined and a smooth regularization is used in the iteratively weighted 3D damped least-square inversion to account for the lateral sensitivity of the surface wave measurements.

The initial reference V_S model follows the previous seismic Pwave study scaled by a constant V_P/V_S of 1.73 (Farrell et al., 2014). During the iterative process, the reference V_S model and the corresponding sensitivity kernels are updated as well as the derivative weighted sum (DWS; Fig. S4), a measure of the 3D spatial sensitivity for the inversion (Huang et al., 2014, 2015). In the inversion, the V_P and density are scaled with Vs based on generalized crustal properties (eq. 9 and eq. 1 in Brocher, 2005). We note that surface waves are mostly sensitive to Vs structure and our inversion result is not very sensitive to both the initial model and the scaling relationship chosen. We set the horizontal grid spacing as 10 km. And for vertical grids, we use 1- and 2-km spacings in the top 10 km and between 10 and 20 km depth, respectively. The vertical spacings are then increased from 6 to 25 km with increasing depth until 160 km. We do not account for topography variation in the inversion considering the mild topography change (\sim 500 m) in Yellowstone relative to the wavelength of the surface waves (mostly much larger than 2 km). We note that the reported depth in this study is relative to the surface, which is \sim 2000 m on average above sea level.

2.5. The joint inversion of Rayleigh and Love waves

We start with independent inversions for Rayleigh and Love waves to retrieve 3D V_{SV} and V_{SH} models, respectively. We ran five iterations to allow the misfit to converge until there were no significant improvements at further iterations. Images of V_{SV} and V_{SH} from independent Rayleigh and Love wave inversions exhibit strikingly distinct structures in the top 15 km (Fig. S5). For example, an elongated low V_{SV} body between 4 and 15 km depth that resembles the upper crustal magma reservoir is largely absent in the V_{SH} model. The V_{SH} model shows a prominent slow structure in the uppermost 3 km depth, whereas the V_{SV} indicates a rather fast velocity compared to the deeper low-velocity body. The discrepancy at 4-15 km depth is likely related to the presence of a sill complex comprising the Yellowstone magmatic system and hence strong positive radial anisotropy (Jiang et al., 2018). However, for the shallower depth, we cannot distinguish whether the difference is from radial anisotropy and/or a mismatched sensitivity. Love waves generally have a shallower sensitivity compared to Rayleigh waves, and thus a joint inversion is desired to leverage the complementary sensitivity (Fig. S3).

To better resolve the anisotropy strength, account for different depth sensitivity of Rayleigh and Love waves, and minimize the trade-off between isotropic and anisotropic parameters, we implemented a two-step inversion scheme to constrain V_{SV} and V_{SH} models for Yellowstone. The first step is a joint inversion combining Rayleigh and Love wave dispersions, but instead of allowing the model space to perturb freely, we require the isotropic velocity to monotonically increase with depth. This step creates a reference model that can satisfy most of the Rayleigh and Love observations (Fig. 5). The damping and smoothing parameters are set through a standard trade-off test (Fig. S6), and we parameterize the weighting factors to have equal weights between Love and Rayleigh waves based on the number of rays (Fig. 3). We monitored the misfit evolution and the optimal model at the 5th iteration yields overall positive and negative misfits for Rayleigh and Love wave measurements, indicating the presence of positive radial anisotropy (V_{SH} >V_{SV}) (Fig. 5).

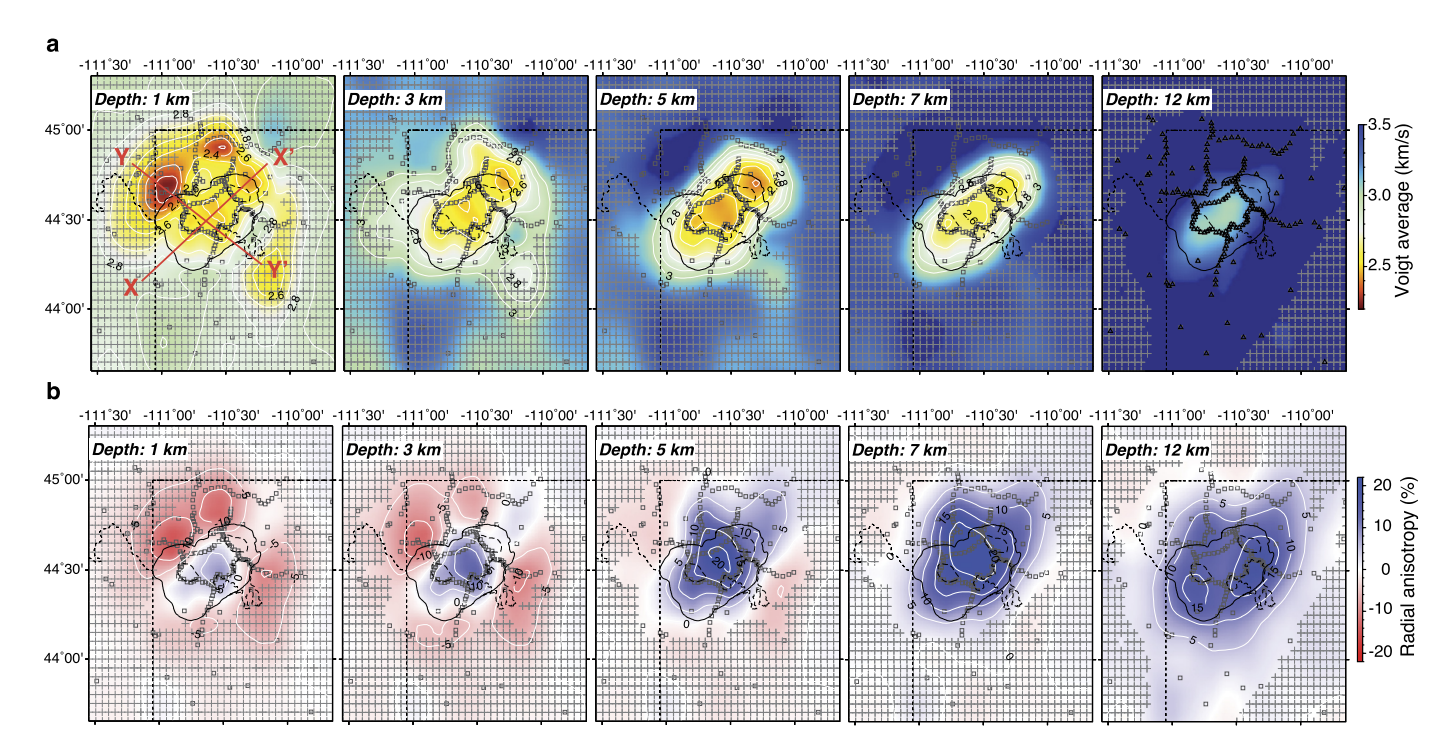


Fig. 6. Shear wave speed and radial anisotropy of Yellowstone's shallow crustal structure. (a) Voigt average velocity and (b) Radial anisotropy depth slides at 1, 3, 5, 7, and 12 km. The red lines mark the cross-sections shown in Fig. 7. The shaded area represents the less-constrained area based on a derivative weighted sum (DWS) threshold shown in Fig. S4. Open squares mark the seismic stations. Solid and dashed lines delineate the 0.63 Ma caldera, resurgent domes, and Yellowstone Lake.

The 3D model resulting from the first joint inversion step is then taken as the initial model for the second step, where Rayleigh and Love waves are inverted separately for V_{SV} and V_{SH} , respectively. Here we allow the model to be perturbed freely without the monotonically increasing constraint to account for all possible structure variations. The damping and smoothing parameters are again set through a standard trade-off test (Fig. S6). Like the previous step, we monitor the misfit evolution and conclude that only one iteration can effectively reduce the misfit with no prominent improvements at further iterations. The inverted V_{SV} and V_{SH} models show significant misfit reductions at all periods compared to the result of the isotropic inversion from the first step (Fig. 5). The radial anisotropy that describes the difference between the two resultant models in 3D space is defined as

Radial anisotropy =
$$(V_{SH} - V_{SV})/V_{VOIGT}$$
, where $V_{VOIGT} = \sqrt{(2V_{SV}^2 + V_{SH}^2)/3}$.

The result of the inverted 3D V_{VOIGT} and radial anisotropy model is summarized in Figs. 6 and 7.

3. Results

3.1. Outside Yellowstone caldera

The Yellowstone caldera boundary delineates distinct geologic formations from the 0.63 Ma caldera-forming eruption: the Lava Creek Tuff (LCT) formation outside and the prevalent rhyolites inside (Christiansen, 2001). The LCT formation was deposited from ash flows during eruptive events and is distributed radially surrounding the caldera (Christiansen, 2001; Finn et al., 2022), consistent with the overall shallow low-V_{VOIGT} and negative anisotropy (V_{SH} < V_{SV}) distributions observed in the top 2 km (Fig. 6). High resistivity (>400 Ω m) is also found for the top 500–1000 m of the LCT formation (Finn et al., 2022), combined with the low Vs, indicating a dry porous medium. Negative anisotropy indicates the

presence of predominantly vertical crack orientations that may result from caldera-wide episodic deformation (Wicks et al., 2006; Chang et al., 2007), or from the local stress induced by the neighboring faulting systems (Christiansen, 2001). Near the NW margin of the caldera, a particularly low-velocity anomaly confined in the top 2 km is illuminated. This anomaly has the lowest V_{VOIGT} of \sim 2.3 km/s and is characterized by -10% radial anisotropy, coinciding with previous observations of low V_P and low V_P/V_S related to the presence of gas-saturated, porous medium (Farrell et al., 2014; Husen et al., 2004).

On the NE margin of the caldera (NE of the Sour Creek resurgent dome; SCD in Fig. 1), we observe a low-velocity anomaly that has the lowest V_{VOIGT} of \sim 2.6 km/s at 1 km depth (Fig. 6). This low-velocity appears to extend to 5-7 km depth but the radial anisotropy transitions from negative to positive around 4 km depth (Fig. 7j). The transition depth is not well-constrained given the mild (<5%) anisotropy strength but the tendency of a sign change likely implies a structural change from shallow vertical fractures to a deeper magmatic sill complex. This area overlaps with the observations of low VP and the largest negative Bouguer gravity anomaly, which was interpreted as the newly-developed structure fueled by hydrothermal fluid and gas following the migration of the magmatic source relative to North American plate motion (DeNosaquo et al., 2009; Farrell et al., 2014). Shallow negative anisotropy found in this study is likely a result of pre-existing ring fractures that facilitate hydrothermal fluid and gas flow. Considering the relatively weak shallow sensitivity of Rayleigh waves, particularly outside of the caldera (Fig. S4), we refrain from further modeling of the observed shallow negative anisotropy, which can be sensitive to crack geometry, temperature, fluid composition, and porosity of the rock matrix (e.g., Bakulin et al., 2000).

3.2. Central Yellowstone caldera

After the 0.63 Ma caldera-forming event, widespread rhyolitic lava was deposited from the center to about ten kilometers SW

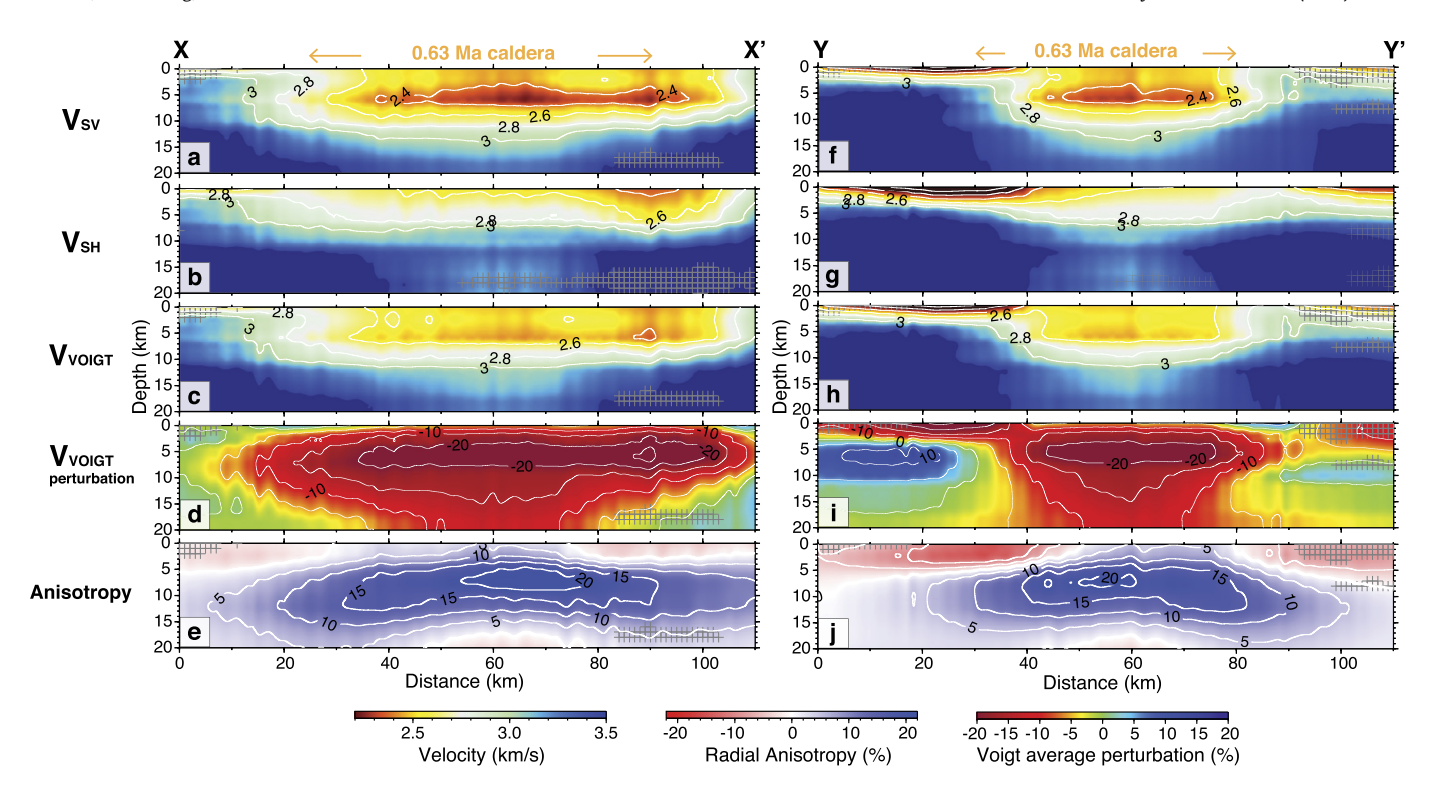


Fig. 7. Cross-sections of the shear wave property of Yellowstone's shallow crustal structure. (a–e) V_{SV} , V_{SH} , V_{VOIGT} , V_{VOIGT} perturbation, and radial anisotropy along the XX' line shown in Figs. 1 and 6. The white lines are the contour lines with an interval of 0.2 km/s for V_{SV} , V_{SH} , V_{VOIGT} , and 5% for V_{VOIGT} perturbation and radial anisotropy. The boundary of the 0.63 Ma caldera is marked at the top. The shaded area represents the less-constrained area based on a derivative weighted sum (DWS) threshold shown in Fig S4. (f–j) similar to (a–e), but for the YY' line shown in Figs. 1 and 6.

outside the caldera. Abundant hydrothermal features with significant elevated heat and gas outlets developed adjacent to the edges of the caldera inner ring fracture (Christiansen et al., 2007). In the top 3 km, our results show a low V_{VOIGT} (~2.5 km/s) situated in the central area of the caldera, but instead of extending outward toward the SW, this low-velocity area is confined within the innercaldera ring fractures (Figs. 1 & 6). This suggests the low-velocity media likely reflects an excess temperature or fracture-dominated regime instead of compositional variability. Tracking the velocity with increasing depth, from 4 km depth, V_{SV} and V_{SH} start to show considerable deviation characterized by >20% positive radial anisotropy (V_{SH} >V_{SV}) (Fig. 7). The strong anisotropy indicates a substantial change in composition or structure, where the structural variability is preferably related to the presence of a magmatic sill complex as proposed for multiple silicic caldera-forming systems (Bastow et al., 2010; Jaxybulatov et al., 2014; Harmon and Rychert, 2015; Jiang et al., 2018; Chambers et al., 2021).

At 5 km depth, we observe the lowest V_{SV} 2.25 km/s and V_{VOIGT} 2.5 km/s with >20% velocity reduction relative to the surrounding crust at the same depth (Fig. 7). The absolute velocity is significantly lower than prior estimates based on sparse array data using ray-based tomography (2.8 km/s by Stachnik et al., 2008 and Jiang et al., 2018) and it is approximately consistent with a recent estimate from Rayleigh wave adjoint tomography (Maguire et al., 2022a). This anomalously low-velocity body outlines a stratified structure between 4 and 7 km depth, where a much subtler velocity anomaly of \sim 10% is observed \sim 7–20 km depth. The entirety of the low-velocity structure from 0-20 km depicts the Yellowstone upper-crustal magma reservoir (Figs. 7d and 7i) with a geometry that is largely comparable with the previous V_P tomography (Farrell et al., 2014; Huang et al., 2015), but with the exception of the depth of the upper boundary. The depth to the top of the reservoir is strikingly 2 km shallower than that resolved by V_P tomography using earthquake data (7 km beneath the surface; Farrell et al., 2014; Huang et al., 2015). Considering the distinct sensitivities of ambient noise surface wave and earthquake body wave measurements, a joint inversion of the two datasets to reconcile the apparent differences and further narrow down the model space will be a focus of future study.

4. Discussion and conclusions

4.1. A low-velocity layer near the top of the upper-crustal magma reservoir

Depicted by our 3D velocity and radial anisotropy model (Fig. 7), the Yellowstone upper-crustal magma reservoir shows a stratified structure between 5 and 20 km depth with an exceptionally slow layer situated near the top (\sim 4-7 km depth). This layer is particularly prominent in the V_{SV} model, and its strong deviation from the V_{SH} model provides distinct insights into magma reservoir organization. The strong positive radial anisotropy constrains the texture of the mushy magma reservoir as dominantly composed of horizontally-elongated melt pockets (Fig. 8). Both isotropic and anisotropic synthetic tests uphold the resolvability of our method for this distinct layering structure, while the limited depth resolution of the surface wave measurements prevented us from accurately resolving layers thinner than 2 km (Supplement material; Figs. S7-S11). We attribute the shallow exceptionally low-velocity layer to the presence of an inhomogeneous accumulation of melt and magmatic volatiles within the upper crustal magma reservoir. The shear velocity is reduced as a result of increasing the bulk volume of liquid or supercritical fluid within the rock matrix and consequently reduced contact area between crystals within the mush (Fig. 8). It is worth noting that no obvious V_{SH} reduction is observed within this shallow layer as V_{SH} waves mostly propagate within the horizontally layered crystalline host rocks and do not need to penetrate the slow concentrated molten magma in between (Figs. 7b and 7g).

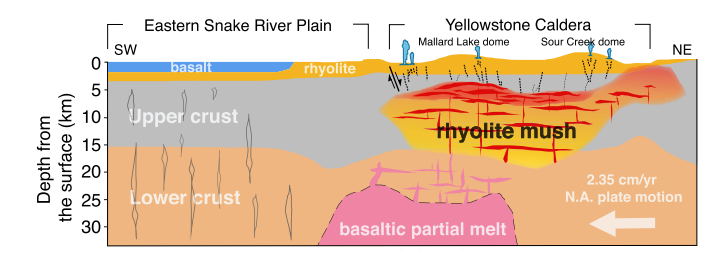


Fig. 8. Schematic model of the shallow Yellowstone crustal structure and magmatic sill complex. The orientation follows and extends the cross-section XX' to the southwest (SW) toward the Snake River Plain. Shapes of structural boundaries are based on Farrell et al. (2014) and Huang et al. (2015). The observed shallow magmatic accumulation is depicted by color gradients and the sill complex is illustrated with textural signatures in the upper-crustal reservoir.

With the higher-resolution images using dense array data, we find that the top of the reservoir exhibits +20% radial anisotropy (V_{SH} >V_{SV}), exceeding the previous estimates of the magnitude of anisotropy by a factor of two (Jiang et al., 2018). We estimate the melt fraction based on a horizontally layered geometry following the effective Vertical Transversely Isotropic (VTI) modeling framework (Postma, 1955; Backus, 1962; Jaxybulatov et al., 2014; Schmandt et al., 2019). VTI considers the observed V_{VOIGT} as the average of a layered 1D medium composed of crystal-rich rock (host rock, high V_{VOIGT}) and crystal-poor rock (molten magma, low V_{VOIGT}), and further searches for optimal parameters of each velocity and the corresponding volume fraction by predicting theoretical V_{SH}, V_{SV}, and radial anisotropy. We constrain the search using information derived from this study, which includes ~20% radial anisotropy, V_{SH} and V_{SV} of the low-velocity layer, and a range of V_{VOIGT} values between 3.2 and 3.8 km/s for crystal-rich rock based on the V_{VOIGT} observation outside the magma reservoir at 5 km depth. The parameterization yields a 30-63% optimal volume fraction for the crystal-poor rock within the sill complex with a range of velocities at 1.55-1.85 km/s (Fig. 9).

The low V_{VOIGT} of the crystal-poor rock is inferred to represent a range of melt fractions from 25-28% based on the velocity-melt relationship from Chu et al. (2010), significantly higher than the bulk averaged estimates derived previously from VP tomography (5-15%, Farrell et al., 2014; Huang et al., 2015) or Vs tomography (16-20%, Maguire et al., 2022a). The theoretical relationship of Chu et al. (2010) was derived assuming an isotropic and melt-filled pore space with an equilibrium pore aspect ratio of 0.35. Presumed temperature of 800–900°C and pressure of 0.1 GPa at \sim 5 km depth were applied based on geochemical estimates (Perkins and Nash, 2002; Vazquez et al., 2009). Note that our estimates may serve as the upper bound as we assume the melt-rich sills are much thicker than the mineral grain size scale (Fig. 8). If the melt pore geometry has a higher aspect ratio, then the same V_{VOIGT} reduction could be achieved with a lower melt fraction (Takei, 2002). Moreover, the melt fraction estimate is likely reduced further with the presence of volcanic volatiles. The proportion of silicate melt and volatiles exsolved from silicate melt may vary within the extremely low velocity upper crustal reservoir. It is worth noting that significant gas and dissolved volatile fluxes are measured in surface settings such as hydrothermal systems, rivers, and soils above the imaged reservoir (Hurwitz and Lowenstern, 2014).

4.2. Implications for Yellowstone's magmatic system

The newly observed low-velocity layer from \sim 4–7 km depth overlaps with petrologic estimates of the depths of magma storage for previously erupted Yellowstone rhyolites. Befus and Gardner (2016) estimated the Central Plateau Member Rhyolites and conclude that CO₂-poor and CO₂-rich magmas were partially crystallized at 2–3 km and 3–6 km depth before eruption. Shamloo

and Till (2019) estimated a storage depth of approximately 5 km from the glass inclusion analysis of the 0.63 Ma LCT. Thus, it appears that melt in the modern system is concentrated at about the same depths as in systems that fed prior eruptions, which likely reflects the crustal rheological properties for a long-lived magmatic system. However, the melt fractions estimated for the modern system (up to \sim 28%) are likely lower than at times preceding prior eruptions given that most erupted rhyolites contained ~35-55% crystal cargo (Marsh, 1981; Costa et al., 2009; Befus and Gardner, 2016; Myers et al., 2016), implying the Yellowstone magmatic system is not currently in an eruptible state. Using the view of Yellowstone's magma concentration and reservoir texture observed in this study, future numerical modeling studies that account for the anisotropy reversal and related stress field could put a more accurate constraint on the evolution of Yellowstone's crustal magmatic system and eruption cycles (Colón et al., 2018). The shallower melt accumulation and hence the shallower heat source indicated by the new shear velocity tomography model may also play an important role in regulating the overlying hydrothermal circulation and geyser dynamics (Duan et al., 1992; Hurwitz and Lowenstern, 2014; Wu et al., 2019). Jointly constraining seismic compressional and shear wave speeds and attenuation as well as understanding compressional wave anisotropy will be important avenues for deciphering fluid and gas fractions of the imaged media to better evaluate the composition of the mushy magma reservoir beneath the Yellowstone caldera.

CRediT authorship contribution statement

All the authors contributed to the design, interpretation, and manuscript preparation of the study. S.-M.W performed the analyses and drafted the manuscript. S.-M.W and H.-H.H develop the 3D inversion code. H.-H.H and F.-C.L. supervised the passive seismic imaging. B.S. supervised the VTI model and melt fraction estimation. F.-C.L., J.F., and B.S. led the project and the nodal field deployment.

Declaration of competing interest

The authors declare that they have no known competing financial interests or personal relationships that could have appeared to influence the work reported in this paper.

Data availability

Broadband seismic data is accessible via IRIS MetaData Aggregator. The Yellowstone Seismic Network (WY: https://doi.org/10.7914/SN/WY). Montana Regional Seismic Network (MB: https://doi.org/10.7914/SN/MB). Plate Boundary Observatory Borehole Seismic Network (PB: https://doi.iris.edu/mda/PB/). United States National Seismic Network (US: https://doi.org/10.7914/SN/US). The nodal data is available on IRIS MetaData Aggregator (network code: 4A; Farrell, 2020; https://doi.org/10.7914/vztw-bx83).

Acknowledgements

This project was funded by: EAR 1753362 & EAR 1950328 & MOST107-2923-M-001-006-MY3. Figures are produced using Generic Mapping Tools (GMT). We thank Dr. James Hammond and an anonymous reviewer for their helpful reviews.

Appendix A. Supplementary material

Supplementary material related to this article can be found online at https://doi.org/10.1016/j.epsl.2023.118244.

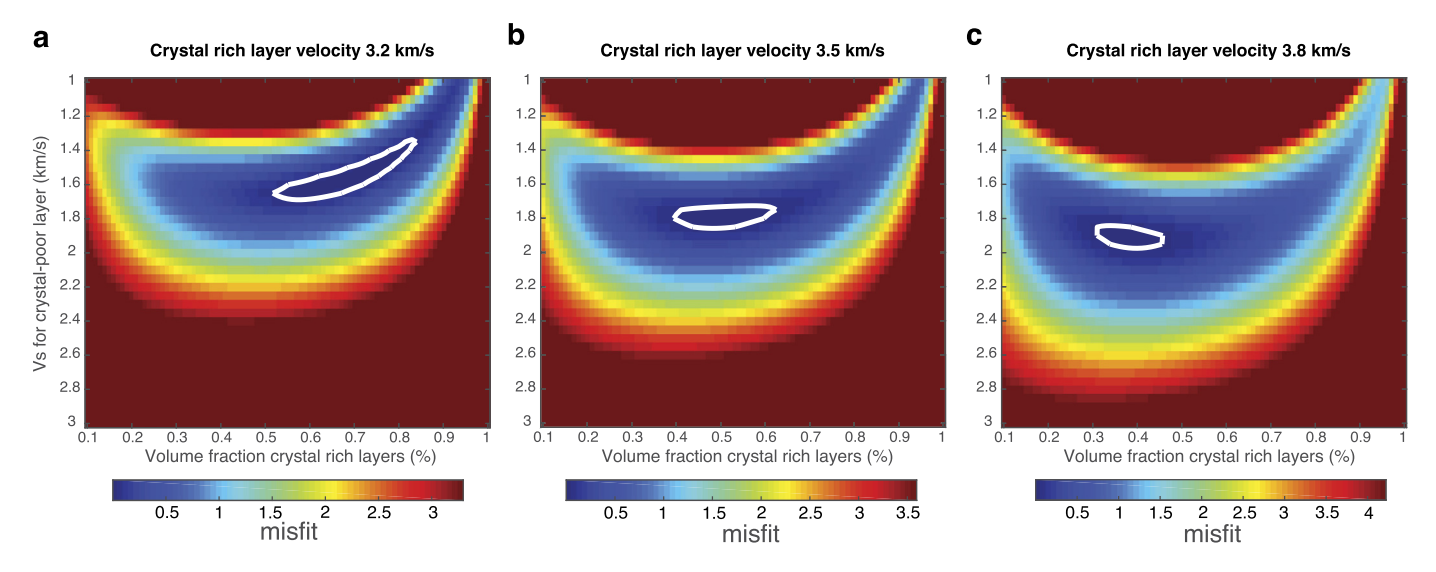


Fig. 9. VTI modeling of melt fraction through grid search for an optimal volume fraction for crystal-rich layer and V_5 for crystal-poor layer. A prior constraint of $\pm 21.57\%$ anisotropy is given based on the inverted model in this study. (a–c) assumptions of crystal-rich layer velocity at 3.2, 3.5, and 3.8 km/s. The misfit is defined as $misfit = (V_{SV}^{obs} - V_{SV}^{pred})^2 + (V_{SH}^{obs} - V_{SV}^{pred})^2 + ((aniso^{obs} - aniso^{pred})/10)^2$, where the superscripts of obs and predict represent the observed and predicted values, respectively. This modeling closely follows Jaxybulatov et al. (2014) and Schmandt et al. (2019). The white contour outlines the area near the global minimum defined as 50 times the lowest misfit

References

Backus, G.E., 1962. Long-wave elastic anisotropy produced by horizontal layering. J. Geophys. Res. 67 (11), 4427–4440.

Bakulin, A., Grechka, V., Tsvankin, I., 2000. Estimation of fracture parameters from reflection seismic data—Part I: HTI model due to a single fracture set. Geophysics 65 (6), 1788–1802.

Barmin, M.P., Ritzwoller, M.H., Levshin, A.L., 2001. A fast and reliable method for surface wave tomography. In: Monitoring the Comprehensive Nuclear-Test-Ban Treaty: Surface Waves, pp. 1351–1375.

Bastow, I.D., Pilidou, S., Kendall, J.M., Stuart, G.W., 2010. Melt-induced seismic anisotropy and magma assisted rifting in Ethiopia: evidence from surface waves. Geochem. Geophys. Geosyst. 11 (6).

Befus, K.S., Gardner, J.E., 2016. Magma storage and evolution of the most recent effusive and explosive eruptions from Yellowstone caldera. Contrib. Mineral. Petrol. 171 (4), 1–19.

Bensen, G.D., Ritzwoller, M.H., Barmin, M.P., Levshin, A.L., Lin, F., Moschetti, M.P., Shapiro, N.M., Yang, Y., 2007. Processing seismic ambient noise data to obtain reliable broad-band surface wave dispersion measurements. Geophys. J. Int. 169, 1239–1260.

Berg, E.M., Lin, F.C., Allam, A., Schulte-Pelkum, V., Ward, K.M., Shen, W., 2020. Shear velocity model of Alaska via joint inversion of Rayleigh wave ellipticity, phase velocities, and receiver functions across the Alaska transportable array. J. Geophys. Res., Solid Earth 125, e2019

Brocher, T.M., 2005. Empirical relations between elastic wavespeeds and density in the Earth's crust. Bull. Seismol. Soc. Am. 95 (6), 2081–2092.

Caricchi, L., Burlini, L., Ulmer, P., 2008. Propagation of P and S-waves in magmas with different crystal contents: insights into the crystallinity of magmatic reservoirs. J. Volcanol. Geotherm. Res. 178, 740–750.

Cashman, K.V., Sparks, R.S.J., Blundy, J.D., 2017. Vertically extensive and unstable magmatic systems: a unified view of igneous processes. Science 355 (6331), eaag3055.

Chambers, E.L., Harmon, N., Rychert, C.A., Keir, D., 2021. Variations in melt emplacement beneath the northern East African Rift from radial anisotropy. Earth Planet. Sci. Lett. 573, 117150.

Chang, W.L., Smith, R.B., Wicks, C., Farrell, J.M., Puskas, C.M., 2007. Accelerated uplift and magmatic intrusion of the Yellowstone caldera, 2004 to 2006. Science 318, 952–956

Christiansen, R.L., 2001. The quaternary and Pliocene Yellowstone plateau volcanic field of Wyoming, Idaho, and Montana. U.S. Geol. Surv. Prof. Pap. 729-G, 145.

Christiansen, R.L., Lowenstern, J.B., Smith, R.B., Heasler, H., Morgan, L.A., Nathenson, M., et al., 2007. Preliminary assessment of volcanic and hydrothermal hazards in Yellowstone National Park and vicinity. U.S. Geol. Surv.

Chu, R., Helmberger, D.V., Sun, D., Jackson, J.M., Zhu, L., 2010. Mushy magma beneath Yellowstone. Geophys. Res. Lett. 37, L01306. https://doi.org/10.1029/ 2009GL041656.

Colón, D.P., Bindeman, I.N., Gerya, T.V., 2018. Thermomechanical modeling of the formation of a multilevel, crustal-scale magmatic system by the Yellowstone plume. Geophys. Res. Lett. 45 (9), 3873–3879.

Costa, A., Caricchi, L., Bagdassarov, N., 2009. A model for the rheology of particle-bearing suspensions and partially Molten rocks. Geochem. Geophys. 10 (3).

DeNosaquo, K.R., Smith, R.B., Lowry, A.R., 2009. Density and lithospheric strength models of the Yellowstone-Snake River Plain volcanic system from gravity and heat flow data. J. Volcanol. Geotherm. Res. 188, 108–127.

Duan, Z., Møller, N., Weare, J.H., 1992. An equation of state for the CH4-CO2-H20 system: II. Mixtures from 50 to 1000 C and 0 to 1000 bar. Geochim. Cosmochim. Acta 56 (7), 2619–2631.

Eddy, M.P., Bowring, S.A., Miller, R.B., Tepper, J.H., 2016. Rapid assembly and crystallization of a fossil large-volume silicic magma chamber. Geology 44 (4), 331–334

Fang, H., Yao, H., Zhang, H., Huang, Y.C., van der Hilst, R.D., 2015. Direct inversion of surface wave dispersion for three-dimensional shallow crustal structure based on ray tracing: methodology and application. Geophys. J. Int. 201, 1251–1263.

Fang, H., Zhang, H., Yao, H., Allam, A., Zigone, D., Ben-Zion, Y., et al., 2016. A new algorithm for three-dimensional joint inversion of body wave and surface wave data and its application to the southern California plate boundary region. J. Geophys. Res., Solid Earth 121 (5), 3557–3569.

Finn, C.A., Bedrosian, P.A., Holbrook, W.S., Auken, E., Bloss, B.R., Crosbie, J., 2022. Geophysical imaging of the Yellowstone hydrothermal plumbing system. Nature 603 (7902), 643–647.

Farrell, J., Husen, S., Smith, R.B., 2009. Earthquake swarm and b-value characterization of the Yellowstone volcano-tectonic system. J. Volcanol. Geotherm. Res. 188, 260–276. https://doi.org/10.1016/j.volgeores.2009.08.008.

Farrell, J., Smith, R.B., Taira, T.A., Chang, W.L., Puskas, C.M., 2010. Dynamics and rapid migration of the energetic 2008–2009 Yellowstone Lake earthquake swarm. Geophys. Res. Lett. 37 (19).

Farrell, J., Smith, R.B., Husen, S., Diehl, T., 2014. Tomography from 26 years of seismicity revealing that the spatial extent of the Yellowstone crustal magma reservoir extends well beyond the Yellowstone caldera. Geophys. Res. Lett. 41, 3068–3073. https://doi.org/10.1002/2014GL059588.

Farrell, J., 2020. Imaging Yellowstone's shallow Magma Reservoir [Data set]. International Federation of Digital Seismograph Networks. https://doi.org/10.7914/vztw-bx83.

Golos, E.M., Fang, H., Yao, H., Zhang, H., Burdick, S., Vernon, F., et al., 2018. Shear wave tomography beneath the United States using a joint inversion of surface and body waves. J. Geophys. Res., Solid Earth 123 (6), 5169–5189.

Harmon, N., Rychert, C.A., 2015. Seismic imaging of deep crustal melt sills beneath Costa Rica suggests a method for the formation of the archean continental crust. Earth Planet. Sci. Lett. 430, 140–148.

Herrmann, R.B., Ammon, C.J., 2004. Surface waves, receiver functions and crustal structure, in Computer Programs in Seismology, Version 3.30. Saint Louis University. Retrieved from http://www.eas.slu.edu/People/RBHerrmann/CPS330. html

Huang, H.-H., Wu, Y.-M., Song, X., Chang, C.-H., Lee, S.-J., Chang, T.-M., Hsieh, H., H., 2014. Joint Vp and Vs tomography of Taiwan: Implications for subductioncollision orogeny. Earth Planet. Sci. Lett. 392, 177–191.

Huang, H.-H., Lin, F.-C., Schmandt, B., Farrell, J., Smith, R.B., Tsai, V.C., 2015. The Yellowstone magmatic system from the mantle plume to the upper crust. Science 348 (6236), 773–776.

- Hurwitz, S., Lowenstern, J.B., 2014. Dynamics of the Yellowstone hydrothermal system. Rev. Geophys. 52 (3), 375–411.
- Husen, S., Smith, R.B., Waite, G.P., 2004. Evidence for gas and magmatic sources beneath the Yellowstone volcanic field from seismic tomographic imaging. J. Volcanol. Geotherm. Res. 131, 397–410.
- Jaxybulatov, K., Shapiro, N.M., Koulakov, I., Mordret, A., Landès, M., Sens-Schönfelder, C., 2014. A large magmatic sill complex beneath the Toba caldera. Science 346 (6209), 617–619.
- Jiang, C., Schmandt, B., Farrell, J., Lin, F.C., Ward, K.M., 2018. Seismically anisotropic magma reservoirs underlying silicic calderas. Geology 46 (8), 727-730.
- Koketsu, K., Sekine, S., 1998. Pseudo-bending method for three-dimensional seismic raytracing in a spherical Earth with discontinuities. Geophys. J. Int. 132 (2), 339–346.
- Koper, K.D., Burlacu, R., 2015. The fine structure of double-frequency microseisms recorded by seismometers in North America. J. Geophys. Res., Solid Earth 120 (3), 1677–1691.
- Lin, F.-C., Moschetti, M.P., Ritzwoller, M.H., 2008. Surface wave tomography of the western United States from ambient seismic noise: Rayleigh and Love wave phase velocity maps. Geophys. J. Int. 173 (1), 281–298.
- Lin, F.-C., Li, D., Clayton, R.W., Hollis, D., 2013. High-resolution 3D shallow crustal structure in Long Beach, California: application of ambient noise tomography on a dense seismic array. Geophysics 78 (4), Q45–Q56.
- Lin, F.-C., Tsai, V.C., Schmandt, B., 2014. 3-D crustal structure of the western United States: application of Rayleigh-wave ellipticity extracted from noise cross-correlations. Geophys. J. Int. 198 (2), 656–670.
- Marsh, B.D., 1981. On the crystallinity, probability of occurrence, and rheology of lava and magma. Contrib. Mineral. Petrol. 78 (1), 85–98.
- Maguire, R., Schmandt, B., Li, J., Jiang, C., Li, G., Wilgus, J., Chen, M., 2022a. Magma accumulation at depths of prior rhyolite storage beneath Yellowstone caldera. Science 378 (6623), 1001–1004.
- Maguire, R., Schmandt, B., Chen, M., Jiang, C., Li, J., Wilgus, J., 2022b. Resolving continental magma reservoirs with 3D surface wave tomography. Geochem. Geophys. 23 (8), e2022GC010446.
- Mordret, A., Rivet, D., Landès, M., Shapiro, N.M., 2015. Three-dimensional shear velocity anisotropic model of Piton de la Fournaise Volcano (La Réunion Island) from ambient seismic noise. J. Geophys. Res., Solid Earth 120 (1), 406–427.
- Myers, M.L., Wallace, P.J., Wilson, C.J., Morter, B.K., Swallow, E.J., 2016. Prolonged ascent and episodic venting of discrete magma batches at the onset of the Huck-leberry Ridge supereruption, Yellowstone. Earth Planet. Sci. Lett. 451, 285–297.
- Pang, G., Koper, K.D., Hale, J.M., Burlacu, R., Farrell, J., Smith, R.B., 2019. The 2017–2018 Maple Creek earthquake sequence in Yellowstone National Park, USA. Geophys. Res. Lett. 46 (9), 4653–4663.
- Perkins, M.E., Nash, B.P., 2002. Explosive silicic volcanism of the Yellowstone hotspot: the ash fall tuff record. Geol. Soc. Am. Bull. 114, 367–381.
- Postma, G.W., 1955. Wave propagation in a stratified medium. Geophysics 20 (4), 780–806
- Schmandt, B., Jiang, C., Farrell, J., 2019. Seismic perspectives from the western US on magma reservoirs underlying large silicic calderas. J. Volcanol. Geotherm. Res. 384, 158–178.

- Shamloo, H.I., Till, C.B., 2019. Decadal transition from quiescence to supereruption: petrologic investigation of the Lava Creek Tuff, Yellowstone caldera, WY. Contrib. Mineral. Petrol. 174, 32.
- Shelly, D.R., Hill, D.P., Massin, F., Farrell, J., Smith, R.B., Taira, T.A., 2013. A fluid-driven earthquake swarm on the margin of the Yellowstone caldera. J. Geophys. Res., Solid Earth 118 (9), 4872–4886.
- Stachnik, J.C., Dueker, K., Schutt, D.L., Yuan, H., 2008. Imaging Yellowstone plumelithosphere interactions from inversion of ballistic and diffusive Rayleigh wave dispersion and crustal thickness data. Geochem. Geophys. 9 (6).
- Stelten, M.E., Cooper, K.M., Vazquez, J.A., Calvert, A.T., Glessner, J.J., 2015. Mechanisms and timescales of generating eruptible rhyolitic magmas at Yellowstone caldera from zircon and sanidine geochronology and geochemistry. J. Petrol. 56 (8), 1607–1642.
- Takei, Y., 2002. Effect of pore geometry on VP/VS: from equilibrium geometry to crack. J. Geophys. Res., Solid Earth 107 (B2). ECV-6.
- Till, C.B., Vazquez, J.A., Boyce, J.W., 2015. Months between rejuvenation and volcanic eruption at Yellowstone caldera, Wyoming. Geology 43 (8), 695–698.
- Tromp, J., Dahlen, F.A., 1993. Variational principles for surface wave propagation on a laterally heterogeneous Earth—III. Potential representation. Geophys. J. Int. 112, 195–209.
- Vazquez, J.A., Kyriazis, S.F., Reid, M.R., Sehler, R.C., Ramos, F.C., 2009. Thermochemical evolution of young rhyolites at Yellowstone: evidence for a cooling but periodically replenished postcaldera magma reservoir. J. Volcanol. Geotherm. Res. 188 (1–3), 186–196.
- Waite, G.P., Smith, R.B., 2002. Seismic evidence for fluid migration accompanying subsidence of the Yellowstone caldera. J. Geophys. Res., Solid Earth 107 (B9). ESE-1.
- Wang, Y., Lin, F.C., Schmandt, B., Farrell, J., 2017. Ambient noise tomography across Mount St. Helens using a dense seismic array. J. Geophys. Res., Solid Earth 122 (6), 4492–4508.
- Wang, Y., Lin, F-C., Ward, K., 2019. Ambient noise tomography across the Cascadia subduction zone using dense linear seismic arrays and double beamforming. Geophys. J. Int. 217 (3), 1668–1680.
- Wells, D., Lin, F.-C., Pankow, K., Baker, B., Bartley, J., 2022. Combining dense seismic arrays and broadband data to image the subsurface velocity structure in geothermally active south-central Utah. J. Geophys. Res., Solid Earth 127, e2022JB024070. https://doi.org/10.1029/2022JB024070.
- Wicks, C.W., Thatcher, W., Dzurisin, D., Svarc, J., 2006. Uplift, thermal unrest and magma intrusion at Yellowstone caldera. Nature 440 (7080), 72–75.
- Wu, S.-M., Ward, K.M., Farrell, J., Lin, F.-C., Karplus, M., Smith, R.B., 2017. Anatomy of Old Faithful from subsurface seismic imaging of the Yellowstone Upper Geyser Basin. Geophys. Res. Lett. 44 (20), 10–240.
- Wu, S.-M., Lin, F.-C., Farrell, J., Allam, A., 2019. Imaging the deep subsurface plumbing of Old Faithful geyser from low-frequency hydrothermal tremor migration. Geophys. Res. Lett. 46 (13), 7315–7322.
- Yao, H., Beghein, C., Van Der Hilst, R.D., 2008. Surface wave array tomography in SE Tibet from ambient seismic noise and two-station analysis-II. Crustal and upper-mantle structure. Geophys. J. Int. 173 (1), 205–219.